Heterogeneous Catalysis

International Edition: DOI: 10.1002/anie.201914950
German Edition: DOI: 10.1002/ange.201914950

Nickel Poisoning of a Cracking Catalyst Unravelled by Single-Particle X-ray Fluorescence-Diffraction-Absorption Tomography

Marianna Gambino, Martin Veselý, Matthias Filez, Ramon Oord, Dario Ferreira Sanchez, Daniel Grolimund, Nikolai Nesterenko, Delphine Minoux, Marianne Maquet, Florian Meirer, and Bert M. Weckhuysen**

Abstract: *Ni contamination from crude oil in the fluid catalytic cracking (FCC) process is one of the primary sources of catalyst deactivation, thereby promoting dehydrogenation–hydrogenation and speeding up coke growth. Herein, single-particle X-ray fluorescence, diffraction and absorption (μXRF-μXRD-μXAS) tomography is used in combination with confocal fluorescence microscopy (CFM) after thiophene staining to spatially resolve Ni interaction with catalyst components and study zeolite degradation, including the processes of dealumination and Brønsted acid sites distribution changes. The comparison between a Ni-lean particle, exposed to hydrotreated feedstock, and a Ni-rich one, exposed to non-hydrotreated feedstock, reveals a preferential interaction of Ni, found in co-localization with Fe, with the γ-Al_2O_3 matrix, leading to the formation of spinel-type hotspots. Although both particles show similar surface zeolite degradation, the Ni-rich particle displays higher dealumination and a clear Brønsted acidity drop.*

Fluid catalytic cracking (FCC) is the leading industrial technology in the production of gasoline and bulk chemicals, such as propylene.[1] The high activity of the FCC catalyst is governed by the interplay of the meso- and macroporous alumina-silica matrix, mixed with a clay binder, and the embedded zeolite microporous active phase. While the γ-Al_2O_3 matrix ensures the pre-cracking of larger hydrocarbons enabling their accessibility to the zeolite pore network, Brønsted acid active sites introduced upon Al insertion in the zeolite framework promote the cracking reaction.[2–4]

The detrimental effect of poisoning metals contamination and the zeolite hydrothermal degradation lead the catalyst to irreversible deactivation.[2] Poisoning metals, such as Fe, Ni and V, are normally contained in the vacuum gas oil (VGO) feedstock and are accumulated in a shell-like manner over time, while the catalyst runs through the reactor-regenerator cycles.[5–14] For this reason, their concentration is a direct indicator of the catalytic age of individual equilibrium catalyst (ECAT) particles.[6] While Fe contributes to surface vitrification of the catalyst, hindering catalyst accessibility, Ni and V promote hydrocarbons (de-) hydrogenation reactions speeding up coke deactivation.[2,6,10,15–18] In this regard, hydrotreatment is a method used to clean up the feedstock from contaminants prior to its injection in the reactor, consisting in the selective hydrogenation of the organic framework (e.g. porphyrin) coordinating poisoning metals in crude oil.[19] Hydrothermal degradation occurs during catalyst regeneration due to the high temperatures and the presence of in situ steam produced during burning of coke and unreacted hydrocarbons.[20,21] These conditions promote zeolite collapse and dealumination, leading to an irreversible drop in Brønsted acidity and cracking performances.[5,22–25] For this reason, zeolite Y is often stabilized with rare-earth (RE) elements (e.g. La) and steaming treatments in order to increase hydrothermal stability.[2]

The spatially resolved interaction of Ni with the FCC catalyst components and its possible role in the zeolite hydrothermal degradation is up to date poorly understood. Ruiz-Martínez et al. compared for the first time the phase transformations occurring between fresh and ECAT single particles: by using a combination of X-ray diffraction and X-ray fluorescence tomography with 5 μm spatial resolution, they highlighted an egg-shell distribution for Ni and V and an egg-yolk distribution for zeolite in the ECAT, thereby correlating zeolite destruction with Ni and V poisoning.[7] A more recent study by van Bokhoven group, correlated metal deposits on the surface with the formation of an outer amorphous silica-alumina (ASA) layer, containing degraded zeolite, hindering reactants accessibility.[26,27] Regarding zeolite phase deactivation, confocal fluorescence microscopy (CFM) after thiophene staining is a powerful approach to track the 3D distribution of the Brønsted acid sites within FCC catalyst particles: in fact, thiophene can selectively react with Brønsted acid sites in the zeolite, forming fluorescent oligomers that can be detected by CFM.[28]

[*] Dr. M. Gambino, Dr. M. Veselý, Dr. M. Filez, Dr. R. Oord, Dr. F. Meirer, Prof. Dr. B. M. Weckhuysen
Inorganic Chemistry and Catalysis
Debye Institute for Nanomaterials Science
Utrecht University
Universiteitsweg 99, 3584 CG Utrecht (The Netherlands)
E-mail: F.Meirer@uu.nl
B.M.Weckhuysen@uu.nl

Dr. D. Ferreira Sanchez, Dr. D. Grolimund
Swiss Light Source, Paul Scherrer Institute
5232 Villigen (Switzerland)

Dr. N. Nesterenko, Dr. D. Minoux
Total Research and Technology Feluy
Zone Industrielle Feluy C, 7181 Seneffe (Belgium)

M. Maquet
Total Research and Technology Gonfreville
Zone Industrielle Carrefour N° 4, BP 27, 76700 Harfleur (France)

Supporting information and the ORCID identification number(s) for the author(s) of this article can be found under: https://doi.org/10.1002/anie.201914950.

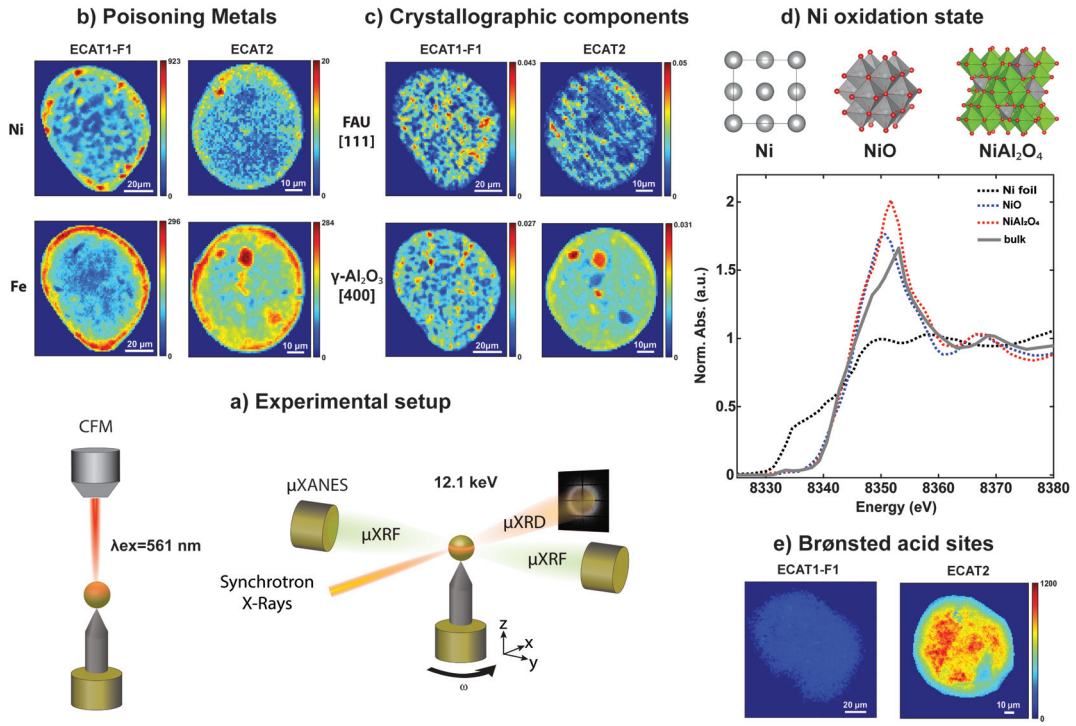

Figure 1. a) Schematic representation of the lab-based confocal fluorescence microscopy (CFM)—after thiophene staining—experiment (left) and μXRF-μXRD-μXANES tomography setup (right) used to collect virtual slices on the same single FCC catalyst particle. A single catalyst particle is mounted on a goniometer. The μXRF signal is measured using two XRF detectors, while μXRD is simultaneously collected using an Eiger 4 m detector. In the same region, μXANES has been measured around the Ni K-edge. X-ray tomography data are acquired in the angular range 0–180°, using a step size of 2°. For each rotation angle a line scan along Y is collected using 1 μm step size. CFM after thiophene staining has been measured on a spherical cap of the catalyst single particle. This setup allowed information to be obtained about b) poisoning metals, in particular Fe and Ni, c) crystallographic phases of the different FCC catalyst components, d) Ni oxidation state and local structure by comparison with Ni, NiO and $NiAl_2O_4$ reference compounds ($NiAl_2O_4$ XANES reference material is taken from literature[29,30]) and e) Brønsted acid distribution.

Herein, we report new physicochemical insights on the interaction of Ni with the FCC catalyst components and assess its role in catalyst deactivation at the single-particle level. Moreover, intra-particle spatial heterogeneities related to zeolite amorphization, dealumination and Brønsted acid sites distribution, have been parallelly investigated to draw a complete deactivation picture. To achieve these goals, we have developed a unique correlative microscopy approach and combined X-ray fluorescence, diffraction and absorption tomography (i.e., μXRF-μXRD-μXAS tomography) with laboratory-based CFM after thiophene staining. Figure 1 summarizes the experimental approach taken (Figure 1 a), and highlights the information obtained (Figure 1 b–e). μXRF-μXRD-μXAS tomography measurements were carried out at the Swiss Light Source (SLS) X05LA microXAS beamline. Since we wanted to assess Ni interaction with the catalyst components we have compared two industrially deactivated particles of approximately the same catalytic age: i) a "Ni-rich" single particle (denoted as ECAT1-F1), exposed in the reactor to non-hydrotreated feedstock and selected from the heaviest fraction F1 of a density separated ECAT batch containing on average 3500 ppm of Ni and 2500 ppm of V; ii) a "Ni-free" particle (denoted as ECAT2) selected from a batch that was exposed to hydrotreated feedstock, with average Ni and V concentration <50 ppm. This particle still contained Fe deposits, presumably from reactor hardware corrosion contamination. Catalyst particles selection was a crucial step for this study: laboratory μXRF analysis allowed to perform a spatially resolved screening of the metal contaminants in ECAT1 and ECAT2 batches and select single particles appropriate for this study. Figure 2 a provides an overview of the poisoning metals content, as obtained from laboratory μXRF, in the unseparated ECAT1, unseparated ECAT2 and in the density sorted F1-F2-F3-F4 ECAT1 fractions. Details about particles selection criteria, batch characterization, experimental procedure and crystallographic phases characterization are explained in the Supporting Information.

This unique set of industrially deactivated samples allowed us to isolate Ni contribution to catalyst deactivation and simulate for the first time the effect of hydrothermal degradation on the zeolite phase in the absence of metals (Ni and V) promoting de-hydrogenation, while still having Fe as indicator of the catalytic age. In fact, Radial Distribution Analysis (RDA) of the μXRF tomography dataset, as shown in Figure 2 b, c, highlighted similar Fe contents in both ECAT1-F1 and ECAT2, thereby suggesting similar catalytic age.[6] On the other hand, Ni displays the same average distribution as Fe in ECAT1-F1, but it is almost absent in ECAT2. Both metals have a maximum concentration at approximately 3 μm from the surface, which is in line with previous studies.[5–8] Despite the similar RDA average ring-

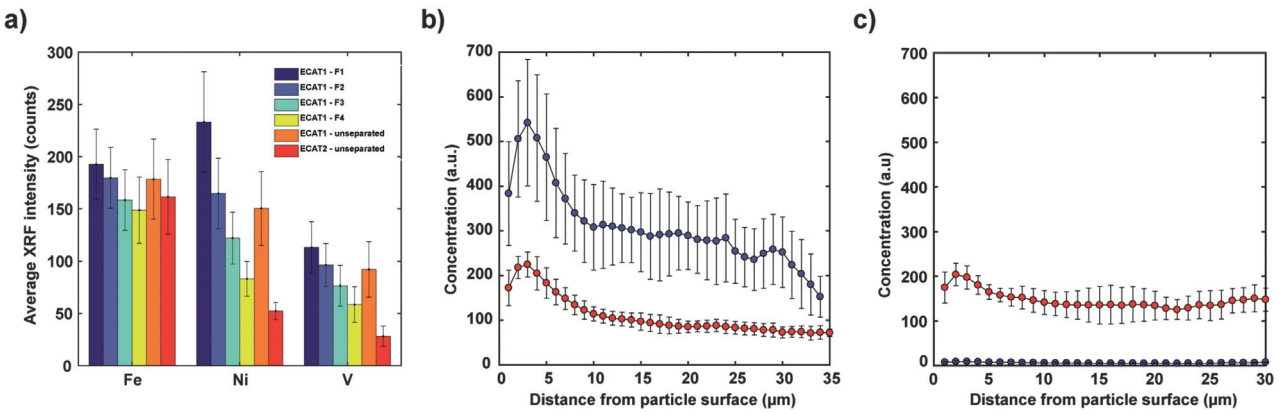

Figure 2. a) Laboratory μXRF pre-characterization of the catalyst materials under study and represented by a histogram distribution showing the average Fe, Ni, V XRF intensity. The samples under study include ECAT-1 and ECAT-2 samples, which are, respectively Ni-rich and Ni-poor. The Ni-rich ECAT-1 sample was then further density separated in four fractions, labelled as F1, F2, F3, and F4, with fraction F1 having the most Ni, while F4 having the least Ni. b) Radial distribution analysis (RDA) plots of the Ni (blue) and Fe (red) distribution, as obtained from the μXRF tomography data, for the ECAT1-F1 and c) ECAT2 samples.

like distribution of Ni and Fe in ECAT1-F1, we observed for the first time the presence of Ni hotspots in high correlation with the γ-Al_2O_3 matrix through the whole particle (Figure 1b,c). Principal components analysis (PCA) and k-means/Gaussian mixture model (GMM) cluster analysis (CA) on γ-Al_2O_3 [400] reflection helped us to rationalize this evidence and compare matrix distribution in presence or absence of Ni (Figure 3a, details in Supporting Information Section S.3.E), while having approximately the same Fe concentration in both particles.[31] While Ni-rich ECAT1-F1 sample formed these γ-Al_2O_3 hotspots, having high spatial correlation with Ni and Fe regions (particularly on the surface), Ni-lean ECAT2 preserved a more uniform matrix distribution, with few γ-Al_2O_3 hotspots and a surface ring mostly correlated with Fe. The red-green-blue (RGB) maps in Figure 3b, respectively show γ-Al_2O_3 (red)–Fe (green)–Ni (blue) and γ-Al_2O_3 (red)–FAU (green)–Ni (blue) overlay maps. It is evident that on the outer surface of the particle Ni, Fe, and γ-Al_2O_3 are highly correlated spatially. However, in the central region, we mainly observe the formation of Ni (blue)–γ-Al_2O_3 (red) hotspots (shown in purple). In this inner region, Fe is present at much lower concentration and is more uniformly distributed. In fact, it is known from literature that in ECAT particles Fe not only exists as Fe^{3+} surface deposit (from VGO feedstock contamination), but it is also naturally contained in lower concentration in the kaolin clay binder as Fe^{2+}.[11] It is also interesting to note how the regions occupied by intact zeolite phase (green) showed no spatial correlation with Ni (Figure S10). γ-Al_2O_3 has a defective spinel structure, with vacancies on the Al^{3+} position to fulfil stoichiom-

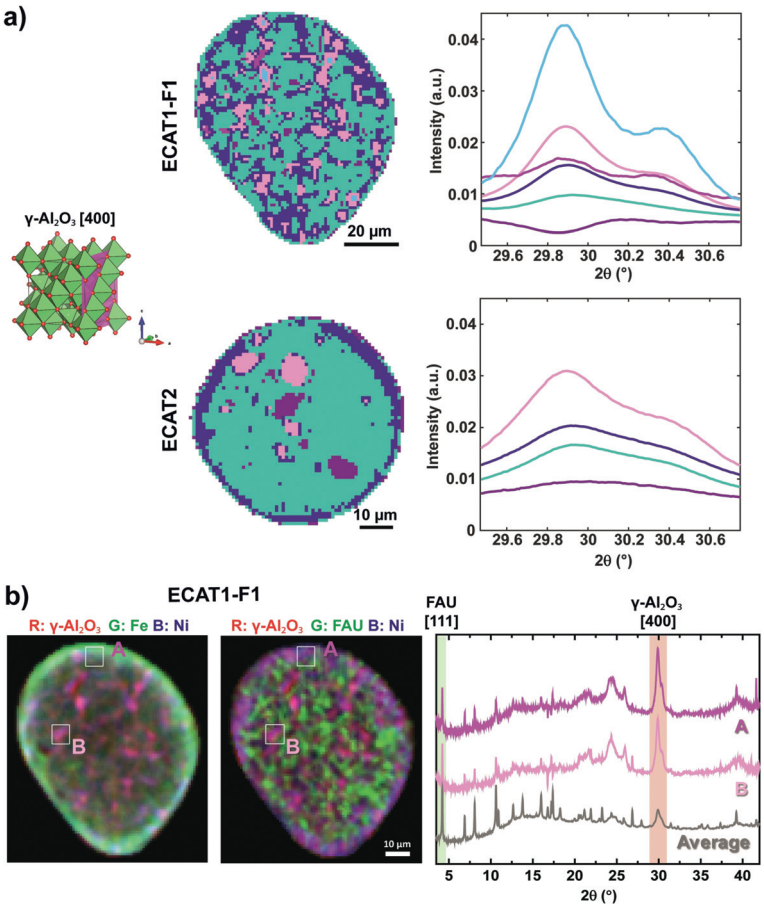

Figure 3. a) Principal component analysis (PCA) and k-means/GMM cluster analysis (CA) results for the spinel [400] X-ray diffraction (XRD) peak of γ-Al_2O_3. Left: image segmentation. Right: average XRD pattern for each cluster. b) Red–green–blue (RGB) overlay (see text for details) of γ-Al_2O_3, Fe, and Ni (left) and γ-Al_2O_3, zeolite Y (with the FAU framework structure), and Ni maps (centre) and average X-ray diffraction (XRD) pattern extracted from the A and B hotspots (where Ni and γ-Al_2O_3 have high spatial correlation) and the average pattern over the whole virtual slice (right) in the sample ECAT1-F1.

etry, belonging to the cubic space group. If we extract the average XRD pattern from the Ni/Fe/γ-Al_2O_3 surface region A and from Ni/γ-Al_2O_3 hotspot B, located in the inner part of the catalyst, and compare these patterns with the virtual slice average pattern (Figure 3b, right), it is evident that both A and B are dominated by the presence of a γ-Al_2O_3 phase. These results strongly suggest a preferential interaction of Ni with the matrix, with surface regions showing a more evident Ni/Fe/γ-Al_2O_3 co-localization.

To further understand the nature of Ni-matrix preferential interaction, we have carried out μXAS tomography at Ni K-edge on the same virtual slice previously measured with μXRD-μXRF tomography. The average XANES extracted over the whole ECAT1-F1 virtual slice was compared with Ni, NiO, and $NiAl_2O_4$ reference compounds (Figure 1d and Figure S9, data analysis details are reported in Section S.3.E). The edge position indicates that Ni is found in the oxidation state 2+ and that metallic Ni is absent. Moreover, the shape of the ECAT1-F1 spectrum and the whiteline position are more similar to the spinel-type $NiAl_2O_4$ reference than NiO, indicating that Ni local structure is compatible with the spinel phase. Since no peak related to Ni or NiO (Section S.3.C, Figure S6a) was clearly detected, we can assume that the majority of Ni, co-localized with Fe in the matrix domains, is mostly incorporated in the γ-Al_2O_3, giving rise to solid solutions retaining the spinel structure. However, although the XANES of the sample is more similar to the $NiAl_2O_4$ reference, there are also small differences between these two spectra, that might be related to the structural complexity of the ECAT. In fact, the matrix is the first phase to be in contact with the feedstock and therefore with different types of poisoning cations. Given the high correlation of Ni and Fe in the surface region, the formation of $Ni(Fe_xAl_{1-x})_2O_4$ mixtures might be possible (see Section S.3.C, Figure S6b). In this case, when also Fe and/or other cations enter the spinel structure, the XANES profile might show some changes compared to pure $NiAl_2O_4$ and the structural disorder around the absorber might increase damping the whiteline intensity, as we observe in ECAT1-F1. Another parameter to consider is also the reactor/regenerator temperature. The highest temperature in the FCC process is reached during regeneration, when coke deposits are burned at around 760 °C. This temperature is too low to form highly crystalline aluminate spinels, that require temperatures above 850 °C to be formed.[32–34] In situ studies related to Ni-containing glasses, also containing other cations, showed that below 800–850 °C the Ni K-edge XANES appears less structured than pure $NiAl_2O_4$ and similar to the XANES reported in Figure 1d and in Figure S9.[35]

Pearson correlation coefficient analysis highly supports this result, as both Ni and Fe are found in high spatial correlation with the spinel phase, corroborating the evidence of a solid-state interaction (Section S.3.F). The high mobility of Ni in solid state structures and its strong tendency to react with γ-Al_2O_3 is well-known in literature:[33,34,36] in fact, $NiAl_2O_4$ spinel is usually formed over γ-Al_2O_3/NiO and/or kaolin reaction and has a similar XRD pattern to γ-Al_2O_3.[37–39] It is also reported that, in presence of Fe_2O_3, NiO and γ-Al_2O_3 $Ni(Fe_xAl_{1-x})_2O_4$ solid solutions can be formed.[32]

However, the temperatures reached during FCC reaction/regeneration cycles, are not high enough to generate high intensity peaks related to highly crystalline phases in the XRD pattern: clear changes in the intensity of the γ-Al_2O_3 XRD peak in Ni-enriched hotspots, together with the indication of a Ni short range structure that is compatible with a spinel structure, pinpoint to a Ni-matrix interaction occurring during FCC. These results indicate that the matrix, essential in the pre-cracking of larger hydrocarbons, acts as a metal trap and helps to passivate Ni in the oxidation state +2, that is not active towards de-hydrogenation. However, although no peaks related to metallic Ni are found in the XRD pattern, we cannot exclude that the 2+ oxidation state is not maintained and can shift to metallic state in the riser, due to the production of H_2.

Despite the exposure to different crude oil feedstocks containing different amounts of metals, both catalyst particles showed similar surface zeolite amorphization. Using La (L_α) map as pristine zeolite distribution marker (Section S.3.G), we observed zeolite collapse on the outer surface (Figure S11), which is obviously more exposed to the feedstock and the harsh reactor conditions, and has a crucial role in providing accessibility to the active sites of the particle core. Moreover, this degraded surface region, is the one where in both samples Fe is accumulated, corroborating what has been previously demonstrated by Ihli et al. about Fe active role in pore clogging and ASA shell formation.[26,27,40,41] Zeolite dealumination was studied by using again PCA and CA, this time by focusing on the zeolite [111] main reflection (Figure 4): the ECAT1-F1 particle, exposed to non-hydrotreated feedstock and therefore rich in Ni, V and Fe, showed a shift in the 2θ position of the [111] XRD peak compared to ECAT2, indicating a higher degree of dealumination. CFM measurements acquired prior to X-ray beam irradiation on a 3D spherical cap of the single particles (Supporting Movies M1 and M2) in the same region of interest where X-ray tomography was carried out, showed that the higher degree of dealumination in ECAT1-F1, exposed to metals rich feedstock, corresponds to an overall drop in Brønsted acidity (Figure 1e). This is in sharp contrast with the ECAT2 sample where a clear fluorescence can be observed after staining the catalyst particle. Moreover, the small angle peak detected for both samples in the 2θ range 0.8–1.8° suggests an overall higher mesoporosity for ECAT2, compatible with less reacted nanosized matrix at negligible Ni concentration. This higher mesoporosity in ECAT2 also means that particle exposed to hydrotreated feedstock would maintain a higher matrix accessibility: this would also contribute, together with the higher Al content in the zeolite framework, to the much higher fluorescence intensity compared to ECAT1-F1, since thiophene oligomers would have more porous space to rapidly expand. ECAT2 also showed an outer layer with reduced mesoporosity that is correlated with Fe distribution and with those regions displaying zeolite amorphization (Section S.3.H).[42,43] These results related to the small-angle peak analysis align well with the pore blocking effect of poisoning metals observed in industrially deactivated ECAT samples and show that the surface regions, where Fe from feedstock contamination is accumulated, exhibit lower mes-

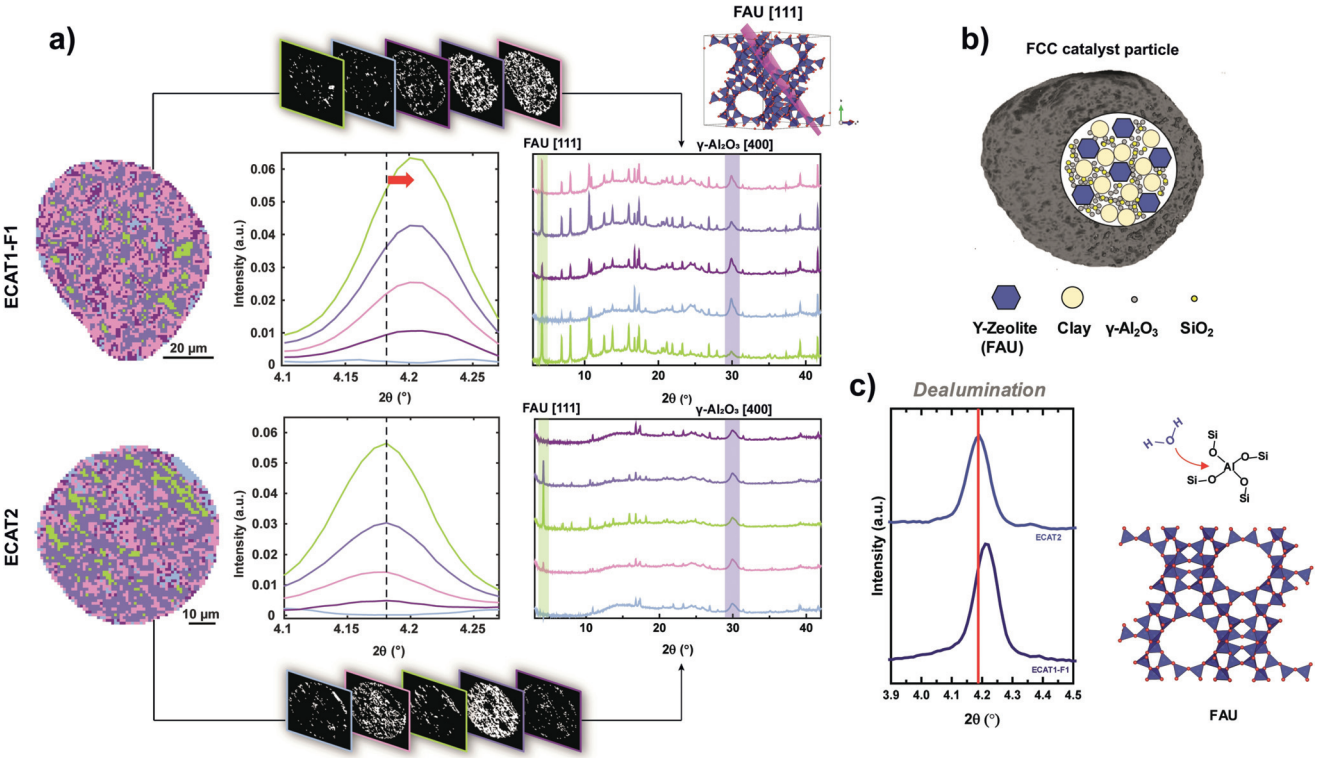

Figure 4. a) Principal component analysis (PCA) and k-means/GMM cluster analysis (CA) results for the [111] X-ray diffraction (XRD) peak for zeolite Y with the framework structure FAU. Left: Image segmentation. Centre: average XRD pattern for each cluster. The vertical dashed line indicates the 2θ position of the FAU [111] peak in ECAT2. The red arrow shows the 2θ shift of the FAU [111] peak in ECAT1-F1 compared to ECAT2. Right: average XRD pattern for each cluster in the whole 2θ range. Binary masks set for each cluster are reported on the top for ECAT1-F1 and on the bottom for ECAT2. The results of filtering the XRD pattern with the clusters binary masks revealed that in the Ni-rich ECAT1-F1 sample, when the zeolite [111] XRD peak intensity decreases, the γ-Al_2O_3 [400] XRD peak intensity increases, while for the ECAT2 sample no matter the variation in the zeolite [111] XRD peak intensity, the γ-Al_2O_3 [400] XRD peak intensity always stays constant. This indicates that in the ECAT2 sample the matrix is more uniformly distributed and mostly unaffected by the metal poisons. b) FCC catalyst components. c) Zeolite [111] reflection shift caused by faujasite dealumination caused by in situ steam formation, occurring during burning of coke and unreacted hydrocarbons. The zeolite dealumination process due to steaming during regeneration is schematized in the structures on the right.

oporosity—in particular those where the small-angle peak shows lower intensity in the Ni-lean particle. On the other hand, the central part of the catalyst, which mostly contains Fe from the clay, maintains high mesoporosity. However, when Ni is also present, the overall intensity of the small angle peak is lower even in the inner part of the catalyst, suggesting that the co-presence of Ni and Fe together causes structural rearrangements in the matrix, possibly leading to reduced mesoporosity.

In conclusion, we have used µXRD-µXRF-µXAS tomography and CFM after thiophene staining as a powerful method to determine the effect of Ni poisoning within real-life FCC catalyst single particles. By simulating the effect of hydrothermal degradation in absence of those metals promoting de-hydrogenation reactions, we observed that Ni preferentially interacts with the alumina phase, forming Ni-rich spinel hotspots. These hotspots help to trap and passivate Ni in the oxidation state 2+, but if Ni oxidation state shifts to metallic during reaction and coke is accumulated in these regions, they might also act as nucleation spots promoting hydrothermal degradation of the zeolite material in the surrounding regions. In this case, as coke and unreacted hydrocarbons are burned during regeneration, the production of in situ steam in the FCC catalyst microstructure would promote zeolite dealumination, leading to an irreversible drop in acidity, cracking activity and catalyst performances. Both FCC catalyst particles showed similar surface zeolite degradation in the same region where Fe and Ni were accumulated, suggesting that the formation of this amorphous silica-alumina shell is most probably an effect of hydrothermal degradation and direct exposure to the harsh regeneration conditions. Therefore, the use of a hydrotreated feedstock is highly recommended in order to extend the lifetime of the catalyst material. The results deriving from single particle analysis also showed the importance of tweaking the matrix composition to trap poisoning metals contained in the feedstock.

Acknowledgements

B.M.W. thanks Total and an European Research Council (ERC) Advanced Grant (grant number 321140) for financial support for this project, while F.M. acknowledges a personal VIDI grant from the Netherlands Organization for Scientific Research (NWO). Total is thanked for providing the FCC

samples. We also acknowledge the Swiss Light Source (SLS) for providing access to microXAS X05LA beamline.

Conflict of interest

The authors declare no conflict of interest.

Keywords: catalyst deactivation · fluid catalytic cracking (FCC) · heterogeneous catalysis · X-ray microscopy · zeolites

How to cite: *Angew. Chem. Int. Ed.* **2020**, *59*, 3922–3927
Angew. Chem. **2020**, *132*, 3950–3955

[1] E. T. C. Vogt, B. M. Weckhuysen, *Chem. Soc. Rev.* **2015**, *44*, 7342–7370.
[2] H. S. Cerqueira, G. Caeiro, L. Costa, F. Ramôa Ribeiro, *J. Mol. Catal. A* **2008**, *292*, 1–13.
[3] A. Corma, A. V. Orchillés, *Microporous Mesoporous Mater.* **2000**, *35–36*, 21–30.
[4] J. Scherzer, *Appl. Catal.* **1991**, *75*, 1–32.
[5] S. Kalirai, P. P. Paalanen, J. Wang, F. Meirer, B. M. Weckhuysen, *Angew. Chem. Int. Ed.* **2016**, *55*, 11134–11138; *Angew. Chem.* **2016**, *128*, 11300–11304.
[6] F. Meirer, S. Kalirai, D. Morris, S. Soparawalla, Y. Liu, G. Mesu, J. C. Andrews, B. M. Weckhuysen, *Sci. Adv.* **2015**, *1*, e1400199.
[7] J. Ruiz-Martínez, A. M. Beale, U. Deka, M. G. O'Brien, P. D. Quinn, J. F. W. Mosselmans, B. M. Weckhuysen, *Angew. Chem. Int. Ed.* **2013**, *52*, 5983–5987; *Angew. Chem.* **2013**, *125*, 6099–6103.
[8] Y. Liu, F. Meirer, C. M. Krest, S. Webb, B. M. Weckhuysen, *Nat. Commun.* **2016**, *7*, 12634.
[9] Q. Wang, G. Giannetto, M. Guisnet, *J. Catal.* **1991**, *130*, 471–482.
[10] F. Meirer, D. T. Morris, S. Kalirai, Y. Liu, J. C. Andrews, B. M. Weckhuysen, *J. Am. Chem. Soc.* **2015**, *137*, 102–105.
[11] A. M. Wise, J. N. Weker, S. Kalirai, M. Farmand, D. A. Shapiro, F. Meirer, B. M. Weckhuysen, *ACS Catal.* **2016**, *6*, 2178–2181.
[12] S. Kalirai, U. Boesenberg, G. Falkenberg, F. Meirer, B. M. Weckhuysen, *ChemCatChem* **2015**, *7*, 3674–3682.
[13] F. Meirer, S. Kalirai, J. Nelson Weker, Y. Liu, J. C. Andrews, B. M. Weckhuysen, *Chem. Commun.* **2015**, *51*, 8097–8100.
[14] S. R. Bare, M. E. Charochak, S. D. Kelly, B. Lai, J. Wang, Y. K. Chen-Wiegart, *ChemCatChem* **2014**, *6*, 1427–1437.
[15] O. Bayraktar, E. L. Kugler, *Catal. Lett.* **2003**, *90*, 155–160.
[16] F. C. Hendriks, S. Mohammadian, Z. Ristanović, S. Kalirai, F. Meirer, E. T. C. Vogt, P. C. A. Bruijnincx, H. C. Gerritsen, B. M. Weckhuysen, *Angew. Chem. Int. Ed.* **2018**, *57*, 257–261; *Angew. Chem.* **2018**, *130*, 263–267.
[17] C. A. Trujillo, U. N. Uribe, P.-P. Knops-Gerrits, L. A. Oviedo, P. A. Jacobs, *J. Catal.* **1997**, *168*, 1–15.
[18] C. R. Moreira, N. Homs, J. L. G. Fierro, M. M. Pereira, P. Ramírez de la Piscina, *Microporous Mesoporous Mater.* **2010**, *133*, 75–81.
[19] J. Ancheyta, P. Morales, G. Betancourt, G. Centeno, G. Marroquín, J. A. D. Muñoz, *Energy Fuels* **2004**, *18*, 1001–1004.
[20] A. S. Escobar, F. V. Pinto, H. S. Cerqueira, M. M. Pereira, *Appl. Catal. A* **2006**, *315*, 68–73.
[21] E. Tangstad, A. Andersen, E. M. Myhrvold, T. Myrstad, *Appl. Catal. A* **2008**, *346*, 194–199.
[22] S. Malola, S. Svelle, F. L. Bleken, O. Swang, *Angew. Chem. Int. Ed.* **2012**, *51*, 652–655; *Angew. Chem.* **2012**, *124*, 676–679.
[23] J. A. van Bokhoven, A. L. Roest, D. C. Koningsberger, J. T. Miller, G. H. Nachtegaal, A. P. M. Kentgens, *J. Phys. Chem. B* **2000**, *104*, 6743–6754.
[24] V. Cadet, F. Raatz, J. Lynch, C. Marcilly, *Stud. Surf. Sci. Catal.* **1989**, *49*, 1377–1386.
[25] A. Nock, R. Rudham, *Zeolites* **1987**, *7*, 481–484.
[26] J. Ihli, R. R. Jacob, M. Holler, M. Guizar-Sicairos, A. Diaz, J. C. da Silva, D. Ferreira Sanchez, F. Krumeich, D. Grolimund, M. Taddei, et al., *Nat. Commun.* **2017**, *8*, 809.
[27] F. Krumeich, J. Ihli, Y. Shu, W.-C. Cheng, J. A. van Bokhoven, *ACS Catal.* **2018**, *8*, 4591–4599.
[28] I. L. C. Buurmans, J. Ruiz-Martínez, W. V. Knowles, D. van der Beek, J. A. Bergwerff, E. T. C. Vogt, B. M. Weckhuysen, *Nat. Chem.* **2011**, *3*, 862.
[29] A. Dugué, O. Dymshits, L. Cormier, B. Cochain, G. Lelong, A. Zhilin, S. Belin, *J. Phys. Chem. Solids* **2015**, *78*, 137–146.
[30] A. Dugué, O. Dymshits, L. Cormier, B. Cochain, G. Lelong, S. Belin, A. Zhilin, *J. Non. Cryst. Solids* **2015**, *413*, 24–33.
[31] Z. Ristanović, J. P. Hofmann, M.-I. Richard, T. Jiang, G. A. Chahine, T. U. Schülli, F. Meirer, B. M. Weckhuysen, *Angew. Chem. Int. Ed.* **2016**, *55*, 7496–7500; *Angew. Chem.* **2016**, *128*, 7622–7626.
[32] K. I. Lilova, K. Shih, C.-W. Pao, J.-F. Lee, A. Navrotsky, *J. Am. Ceram. Soc.* **2012**, *95*, 423–430.
[33] C. Jiménez-González, Z. Boukha, B. de Rivas, J. R. González-Velasco, J. I. Gutiérrez-Ortiz, R. López-Fonseca, *Energy Fuels* **2014**, *28*, 7109–7121.
[34] J. L. Rogers, M. C. Mangarella, A. D. D'Amico, J. R. Gallagher, M. R. Dutzer, E. Stavitski, J. T. Miller, C. Sievers, *ACS Catal.* **2016**, *6*, 5873–5886.
[35] L. Cormier, B. Cochain, A. Dugué, O. Dargaud, *Int. J. Appl. Glas. Sci.* **2014**, *5*, 126–135.
[36] A. Vamvakeros, S. D. M. Jacques, M. Di Michiel, D. Matras, V. Middelkoop, I. Z. Ismagilov, E. V. Matus, V. V. Kuznetsov, J. Drnec, P. Senecal, *Nat. Commun.* **2018**, *9*, 4751.
[37] K. Shih, J. O. Leckie, *J. Eur. Ceram. Soc.* **2007**, *27*, 91–99.
[38] C. Liu, Y. Deng, Y. Pan, S. Zheng, X. Gao, *Appl. Catal. A* **2004**, *257*, 145–150.
[39] S.-J. Yang, Y.-W. Chen, C. Li, *Appl. Catal. A* **1994**, *115*, 59–68.
[40] J. Ihli, D. Ferreira Sanchez, R. R. Jacob, V. Cuartero, O. Mathon, F. Krumeich, C. Borca, T. Huthwelker, W.-C. Cheng, Y. Shu, et al., *Angew. Chem. Int. Ed.* **2017**, *56*, 14031–14035; *Angew. Chem.* **2017**, *129*, 14219–14223.
[41] J. Ihli, A. Diaz, Y. Shu, M. Guizar-Sicairos, M. Holler, K. Wakonig, M. Odstrcil, T. Li, F. Krumeich, E. Müller, et al., *J. Phys. Chem. C* **2018**, *122*, 22920–22929.
[42] S. M. Morris, P. F. Fulvio, M. Jaroniec, *J. Am. Chem. Soc.* **2008**, *130*, 15210–15216.
[43] S. D. M. Jacques, M. Di Michiel, A. M. Beale, T. Sochi, M. G. O'Brien, L. Espinosa-Alonso, B. M. Weckhuysen, P. Barnes, *Angew. Chem. Int. Ed.* **2011**, *50*, 10148–10152; *Angew. Chem.* **2011**, *123*, 10330–10334.

Manuscript received: November 23, 2019
Accepted manuscript online: December 30, 2019
Version of record online: January 23, 2020

